nature photonics

SUPPLEMENTARY INFORMATION

DOI: 10.1038/NPHOTON.2014.323

Swept confocally-aligned planar excitation (SCAPE) microscopy for high-speed volumetric imaging of behaving organisms

Matthew B. Bouchard[1], Venkatakaushik Voleti[1], César S. Mendes[3], Clay Lacefield[4], Wesley B. Grueber[5], Richard S. Mann[3], Randy M. Bruno[2,4] and Elizabeth M. C. Hillman[1,2*]

[1]Laboratory for Functional Optical Imaging, Departments of Biomedical Engineering and Radiology, Columbia University, New York, NY 10027
[2]Kavli Institute for Brain Science, Columbia University, New York, NY 10027
[3]Mann Lab, Department of Biochemistry and Molecular Biophysics, Columbia University, New York, NY 10032
[4]Bruno Lab, Department of Neuroscience, Columbia University, New York, NY 10032
[5]Department of Physiology and Cellular Biophysics, Department of Neuroscience, College of Physicians and Surgeons, Columbia University Medical Center, New York, NY 10032

*corresponding email: eh2245@columbia.edu

Table of Contents:

Supplemental Methods

SCAPE prototype design and optical path

As shown in Supplemental Figure 1, SCAPE is currently implemented using a 12-sided polygonal scanning mirror (Lincoln Laser, DT-12-138-043) custom-mounted on a galvanometer motor (6240HA, Cambridge Technology). Since SCAPE acquires one whole volume per single facet sweep, the polygon is not spun, but bidirectionally scanned back and forth over a relatively small angular range, overcoming the duty-cycle limitations of large facets while maintaining sufficient mirror surface area for reasonable throughput. Controlling this motion using a galvanometer allows precisely synchronized camera acquisition relative to mirror motion: the galvanometer is driven by a DAQ analog output board whose clock is driven by the camera's frame capture signal, although at high imaging speeds, the polygon's motion can be considered continuous. While only two facets of the polygon are actually used, the balance of a low-inertia polygon is preferable to mounting (for example) a pair of mirrors or a mirrored prism.

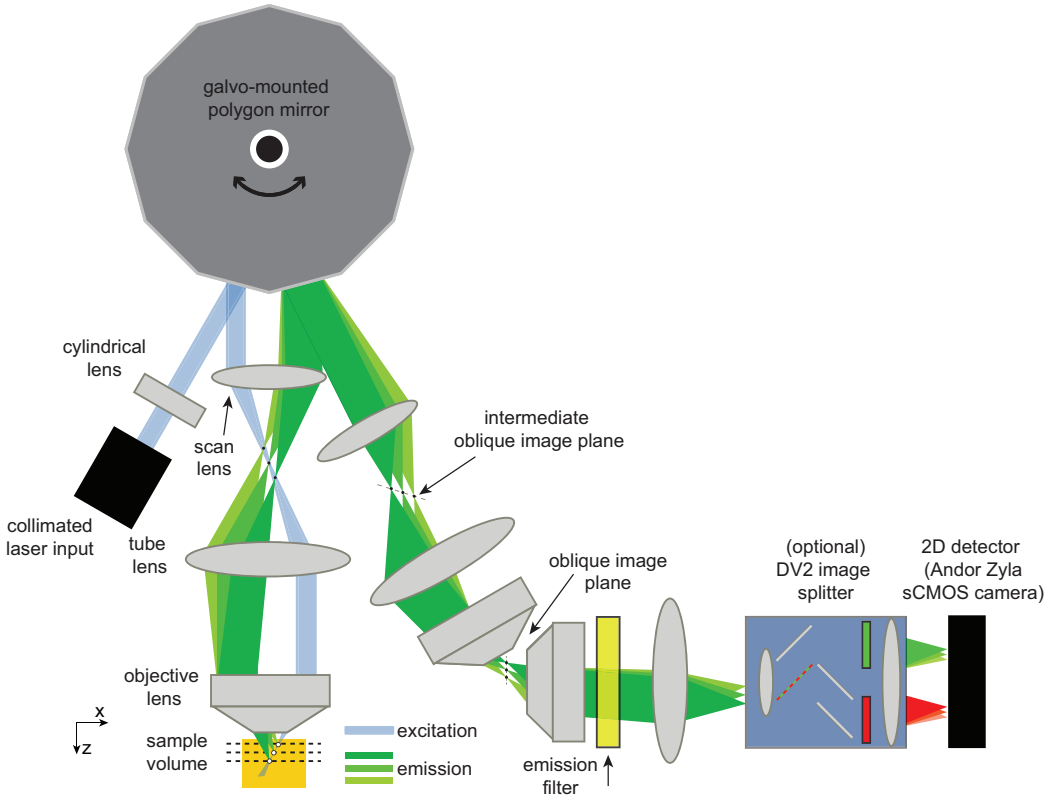

Supplemental Figure 1. Full schematic of current SCAPE system. A scanning polygon mirror sweeps the oblique light-sheet through the sample volume (blue rays), and de-scans returning light such that images of the moving fluorescence plane (green rays) remain focused on a stationary 2D camera. The only moving component is the slowly oscillating polygon mirror.

All data shown used a 30 mW, 488 nm laser (Melles-Griot, 85-BCD-030-115), with optical power at the sample of between 0.5 and 5.05 mW (dependent on sample brightness, desired scan speeds and photosensitivity of the sample). After beam alignment mirrors, a 5x anamorphic telescope composed of two cylindrical lenses unidirectionally expands the beam

before creation of the light sheet with a further 50 mm focal length cylindrical lens (Thorlabs, LJ1695RM-A, LJ1267RM-A and LJ1695RM-A respectively). 8x beam expansion was utilized for phantom and mouse vasculature measurements shown in supplemental section 2, replacing lens LJ1267RM-A with LJ1363RM-A). This incoming beam is incident on the center of one polygon facet, at an angle such that, at the center of the scan sweep, the beam is offset, but perpendicular to the front surface of the scan lens (this angle is a function of the number of facets in the polygon). A scanning telescope is then used to image the reflected beam onto the edge of the back aperture of the objective lens to create an oblique illumination plane within the sample. This beam should be focused at the edge of the true front aperture of the objective, a plane which should also be conjugate to the polygon facet [1]. The scanning telescope uses AC254-050-A1 and AC508-100-A1 lenses, with magnification chosen to maximize the use of the objective lens' numerical aperture (NA), and so should be equal to the ratio of the objective's back aperture diameter and the distance between the centers of two adjacent polygon facets. All images shown here were acquired using an Olympus XLUMPlanFL 20x/0.95W or /1.0W objective lens, although other objective lenses, and even achromatic doublets can be used to provide highly adaptable numerical apertures, working distances and fields of view (with appropriate adjustment of the scan telescope to maintain the conditions above). Changes in objective NA will alter resolution both through alteration of the intersection angle between the incident and detected light, and changes in the individual excitation and emission point spread functions, see supplemental section 1).

Fluorescence emission light emerging from the objective back aperture is mapped back through the scanning telescope and onto an adjacent facet of the polygonal mirror. The polygon de-scans this light into the stationary detection arm. In our current system, the first two lenses of this arm are identical to those within the scan arm telescope (in order from polygon: Thorlabs, AC254-050-A1 and an AC508-100-A1). The light emerging from this telescope can be focused into an oblique plane, corresponding to an image of the illuminated plane within the object being imaged. Following the method of Dunsby [2], we use a pair of objective lenses to create and then rotate this plane. Using objective lenses here provides the necessary NAs and short working distances to achieve plane this rotation while still capturing the detected light. This objective pair is currently an Olympus UPlanSApo 20x/0.75NA and, for adjustable magnification, either an Olympus, LCPlanFL 20x/0.40NA (used for the data shown in figures 2-4 and supplemental figures 6-7) or an Olympus, UPlanFL N 10x/0.30 NA (used for data shown in Figure 5). Light from this last objective lens is focused onto a high-speed sCMOS camera using a final lens (Thorlabs, AC508-075-A).

For fluorescence imaging, excitation light was blocked using a 500 nm long pass filter (Semrock, FF01-496/LP-25) positioned in the collimated space in front of the camera after the oblique image plane had been optically rotated. For dual-color imaging, a 2-channel commercial image splitter (Photometrics DV-2) was inserted, spectrally separating the rotated image plane and repositioning two relayed images side by side onto the camera chip. A green/red filter cube was used in this case, consisting of a Chroma 565dcxr dichroic filter and 525 ± 25 nm and 600 ± 25 nm bandpass filters (86984 and 84785 Edmund Optics, respectively).

For the images shown here, an Andor Zyla sCMOS camera (Zyla-5.5-CL10) was used, operated using the Andor proprietary software installed on a high performance desktop with

a 1 Tb solid state hard drive (for high speed data streaming). The galvanometer-mounted polygonal mirror's motion was controlled via a National Instruments analog input/output board, synchronized to the camera's frame-grab signal. A simple graphical user interface (GUI) written in Matlab™ was used to generate scan patterns, triggered and monitored camera streaming and galvanometer position signals, controlled laser shutters and animal stimulation (where used).

Our prototype SCAPE system is not optimized for aberrations due to the off-axis propagation of light through standard lenses, or for throughput and field of view. Numerous improvements, guided by our simulations, will allow a larger active area of illumination. Our modeling also demonstrates that sampling the 'full aperture' of light emerging from the sample could improve resolution and throughput dramatically (see Supplemental Figure 4), a modification that would remove the polygon scanner (which descans only half of the returning light) and would employ one or two separate scanning elements (e.g. see supplemental section 1 and Supplemental Figure 5). SCAPE thus could also utilize MEMs technology (also suitable for miniaturization) and spatial light modulators (which could also provide improved beam shaping, structured light, STED patterning and adaptive optics corrections) and acousto-optic deflectors for scanning and / or descanning. For two-photon implementations, a further scanning mirror could be used to generate the incoming light sheet from a low-NA beam, such that one line-scan (generating a sheet) fills one camera frame (achievable up to 4,000 LPS for standard galvanometers, fitting well to ~2,000 FPS camera acquisition, assuming sufficient illumination power). A regenerative amplifier could also be used to generate very high energy pulses at lower repetition rates than a standard Ti:Sapphire laser, such that two-photon excitation could be achieved with full light sheet illumination, e.g. 2 kHz pulses could be used to provide one full-sheet pulse per camera frame.

Methods for in-vivo two-photon microscopy comparison

Two-photon microscopy data for comparison to SCAPE was acquired using our home-built two-photon microscope system [3]. The system utilizes a MaiTai HP laser, and three spectrally-resolved R3896 Hamamatsu photomultiplier detectors. The two-photon data shown in Figure 2e, Supplemental Figure 7 and Supplemental Movie 2 were acquired with a 505-560nm emission filter and 800 nm excitation of FITC-dx and an Olympus XLUMPlanFl 20 x/0.95W objective. Two-photon images shown were acquired with 400 x 400 x-y pixels corresponding to a 750 micron field of view, at 3 micron depth steps.

The comparison SCAPE data (shown in Figure 2e, , Supplemental Figure 7 and Supplemental Movie 2) was acquired using 0.4 mW of 488 nm laser light. A slow scan with 300 angular positions (x'), and a 1000 x 500 pixel (y'- z') planes (corresponding to a 924 x 667 x 375 micron (x-y-z) volume) was acquired with a 250 ms integration time per plane to maximize signal to noise (although similar contrast at 200 microns was seen with 2.4mW illumination and a 2.9 ms integration time at 10 VPS). To improve dynamic range, a strip of 50% reflecting plastic film was positioned between the polygon and detection arm to attenuate signal originating from the very surface of the brain. This kind of spatially-dependent attenuation is effective since the position of shallow v/s deep signal on the camera stays constant throughout a scan.

To enable direct comparison to two-photon imaging, SCAPE data was corrected for depth-dependent skew caused by the angle of the oblique light sheet. This was achieved by selecting a skew angle (for both y and x directions) and laterally shifting frames at successive depths by a constant linear factor. Two-photon data was digitally rotated, and both data sets were cropped to match their regions of interest.

SCAPE System Calibration

Calibration factors for our current SCAPE system were measured after each imaging experiment using the following methods. While these calibrations do not formally convert the SCAPE space into Cartesian space, they do result in real (micron) dimensions along each axis.

Depth Axis Calibration:

The oblique sheet was focused onto a flat surface coated in fluorescent tape. The sample was translated along the depth dimension (z) using a micromanipulator stage in increments of 1/1000th of an inch, and image displacement along the camera chip (in the depth direction) was calculated in pixels. Using this calibration factor converts pixel space in z' to real depth within the sample z.

Lateral Axis Calibration:

A standard microscopic test sample (in this case, a fluorescently stained Convallaria stem slice) was imaged with the system. The sample was translated along the lateral dimension (y) using a micromanipulator stage in increments of 1/1000th of an inch. Image displacement along the camera chip (in the y direction) was calculated in pixels. Using this calibration factor converts lateral pixels into real distance in y.

Scan Axis Calibration

Assuming even angular spacing between consecutive frames in a single volume, the scan-axis conversion factor is calculated from two sets of measurements of a standard microscopic test sample (in this case, a fluorescently stained Convallaria stem slice). First, a high resolution volume scan of the sample is acquired over the maximum angular range of the polygonal scanner (at 0.01 volumes / sec). Then, with the illumination plane fixed in a central location, the same sample is physically translated in the x dimension using a micromanipulator stage, acquiring images at increments of 1/1000th of an inch. The two data sets are then compared across the scan range to determine the physical translation (in microns) that equates to 1 degree of angular scan of the polygon (defined as constant K, with units of μm/deg). For a given data set, the conversion factor is then given by:

$$Conversion\ Factor\ \left({}^{\mu m}/_{step}\right) = K * \frac{Total\ polygonal\ scan\ angle}{Number\ of\ steps\ per\ volume}$$

Using this calibration factor converts angular steps into real distance in x.

In-vivo data analysis methods

Dendrite analysis (mouse):

Color-coded dendritic trees shown in Figure 3c were generated by first searching the 4D data set for neuronal events. Maps of the peak of each event, relative to 10-20 frames before the peak were used to identify the location of firing dendrites, and time-courses were extracted from these pixels as a representation of other events in the same neuron. Maps for each firing event for a given neuron were then compared and sorted to ensure that each identified event corresponded to the same neuron. These matched neurons were then averaged over all events to generate a 3D map of a given temporally correlated dendritic tree. Each averaged volume was rendered using the Volren function in Amira and given a unique colormap. Time-courses extracted from the location of the peak pixel in each map are plotted (as raw, unfiltered data) in Figure 3d.

Analysis of intradendrite dynamics in Figure 3e-f was performed using Matlab™. Raw data was first low pass filtered at 1.5 Hz and then a time-window surrounding a particular neuronal event was identified, along with the time of the event's peak. Voxel time-courses were normalized to the start of this time-window, and then the log of each time-course for the rising (up to the peak) and decay (down from the peak) slopes were fit to a linear function. The reciprocal of the gradient of this fit was recorded as onset or decay tau for each voxel respectively. Voxels in which the peak value did not exceed a predetermined threshold were set to zero. The resulting volumetric maps of taus were visualized in Amira™ using the 'physics' colorscale. Voxels for further interrogation and time-course extraction were identified by visualizing individual slices of the tau volumes in Matlab™.

Neuronal tracking algorithm (Drosophila larvae)

Neuronal tracking shown in Figure 5e was performed in Matlab™ and was achieved by first spectrally unmixing the pure green signal of GFP neuronal subset from the mixed emission signal of the larva's gut [3]. The location of a neuron at the start of the time-sequence was then chosen manually from a maximum intensity projection over depth (z'). Sequential frames were then analyzed to identify the point of peak intensity within a selected radius of the starting point, first from a maximum intensity projection over depth (finding y' and z'), and then finding the location of this peak intensity as a function of x' within a column defined by y' and z'. The 'start' location was then updated before moving to the next frame. The process was supervised to ensure no errors, but proceeded in almost real time.

Supplemental Section 1:

SCAPE simulations and optical resolution

Scan / descan geometry

Our current bench-top SCAPE system was built using off-the-shelf components that are not optimized for off-axis transmission. So while demonstrating proof of principle, our measurements do not capture the theoretical limits of SCAPE's performance. To fully understand these limits, we developed several computational models of the SCAPE system. The first is an OpTalix^{TM} model of SCAPE, which is used to demonstrate how SCAPE's descanning geometry allows the system's moving illuminated plane to be mapped onto a stationary camera. One model was generated based on our current system's exact lenses, including a full model of the Olympus XLUMPlanFl 20 x/0.95W objective, while another model was generated using the thin lens approximation, and included a 30 mm focal length, 1" diameter lens as the system's objective. The simulation identifies the location of the light sheet in object space for a given polygon rotation angle, and then maps that illuminated plane to the descanned intermediate oblique image plane (see Figure 1a).

As shown in Supplemental Figure 2 below, the thin lens example shows that the illumination sheet can be descanned almost perfectly to a stationary intermediate oblique image plane (note also the very large achievable field of view). Given the 1x magnification of the system, this plane has the same oblique angle in conjugate image space (with respect to the last lens) as the excitation sheet in object space at 0 degree rotation of the polygon. For the real-lens case, with an Olympus XLUMPlanFl 20 x/0.95W objective, the descan pattern is also adequate, although it has around 20 microns of wobble at the edges resulting from to the field curvature of the real achromatic lenses, and the slight translation of the polygon. In practice, this wobble would defocus the descanned image on the camera, an effect that would be lessened for lower NA detection paths. The field of view in the Olympus XLUMPlanFl 20 x/0.95W objective case is also limited by aperturing within the lens of light entering the edge of the lens with incident angles of greater than 90 degrees (shifting the field of view off-center).

These simulations also demonstrate the overall angular scan pattern of SCAPE, revealing an expected distortion from Cartesian space. All data shown in this article (except Figure 2e) are uncorrected for this pattern, and exhibit little noticeable scaling. However, system-specific models such as these could be readily used to map this distorted measurement space onto 3D Cartesian space if absolute dimensional measurements are required.

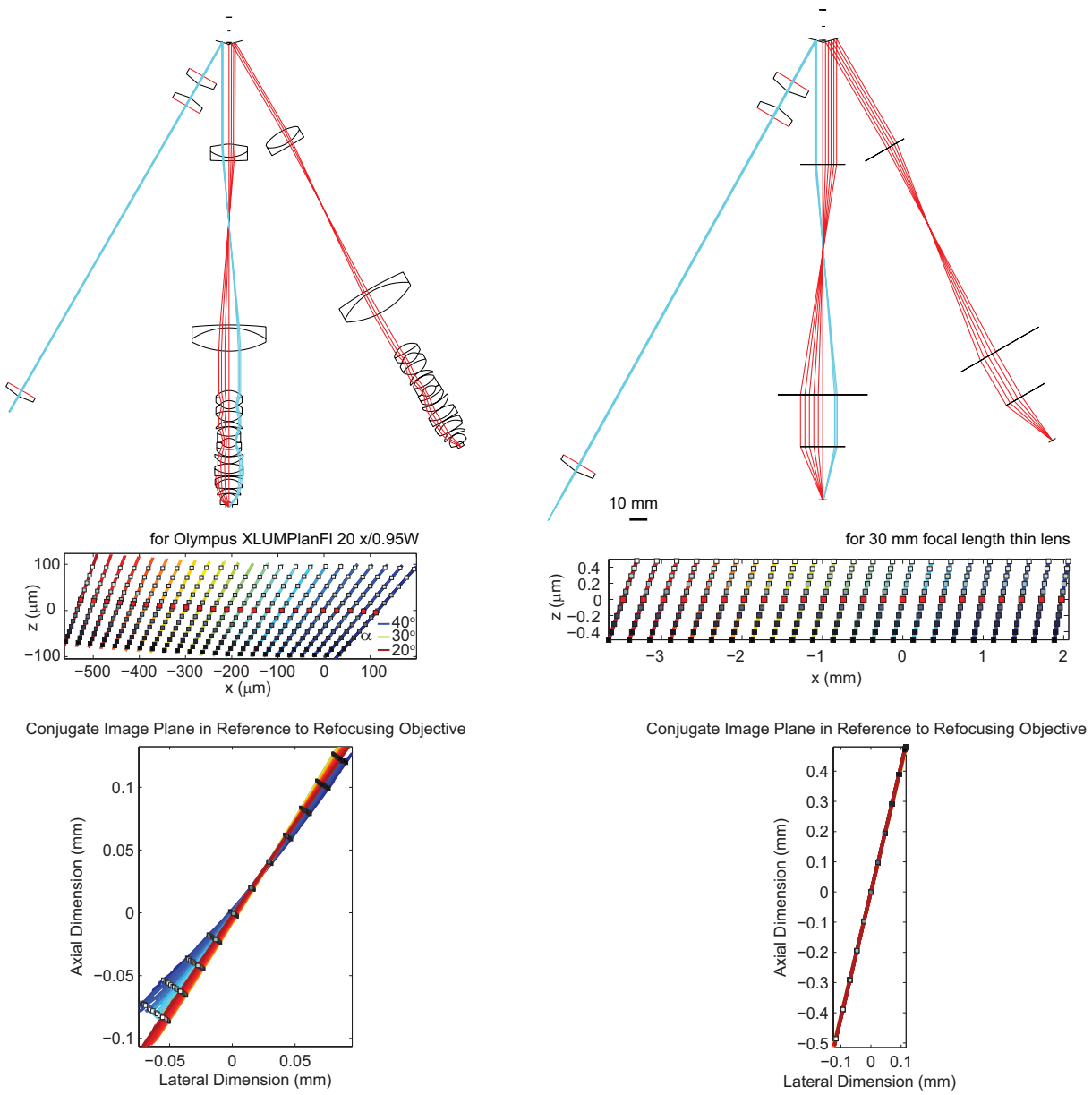

Supplemental Figure 2. Optalix simulations of the SCAPE optical geometry for 'real' lenses and a Olympus XLUMPlanFl 20 x/0.95W objective (left) and ideal thin lenses and a 30 mm focal length 1" diameter lens as the system's objective (right). Both figures show the beam path for 0 degree polygon rotation, and map to the intermediate oblique image plane (model does not include the subsequent image plane rotation optics). The central plots show the sampling positions of the sweeping sheet in object space, with each color representing a different polygon angle, and each square representing a pixel on the camera (mapped to the intermediate oblique image plane). The red squares correspond to the focal point of the excitation beam as it sweeps through object space. The descanned representations of these same points at the intermediate oblique image plane are shown below for both cases. These are oriented with respect to the front face of the last lens before the intermediate oblique image plane. The thin lens example shows near-perfect descanning, while the 'real lens' case shows up to 20 microns of wobble at the edges of the field corresponding to the imperfect behavior of the real lenses used, and the imperfect rotation of a polygon's mirror facets. The angles of these image planes govern the rotation angle of the final camera telescope (not shown).

Optical resolution

Next we consider the diffraction-limited resolution of SCAPE utilizing two different models. The first model was based on a 3D Fourier optics analysis[4], following the method of Engelbrecht and Stelzer for calculation of a light-sheet imaging point spread function [5], and was used to generate the point spread function shown in Figure 1e. This model was based on the geometry of the Olympus XLUMPlanFl 20 x/0.95W lens (2 mm WD, 2.3 mm radius front aperture) for the 0-degree scan angle, at z = 0 depth plane (corresponding to the focal plane of the objective) and incorporated off-axis apertures at the pupil plane to generate an aberrated excitation light sheet (488 nm) and a detection point (530 nm) corresponding to our 'half aperture' polygon geometry $p_e = a/2$ as defined below in Supplemental Figure 3a. Note that this model did not consider the additional effects of the image rotation optics in the detection side of SCAPE, which may further reduce the point spread function (PSF) size in practice. Supplemental Figure 3b illustrates how this system PSF was assembled. Supplemental Figure 3c shows the x-direction and z-direction cross-sections through the point spread function for both half-aperture ($p_e = a/2$) and full-aperture ($p_e = a$) detection.

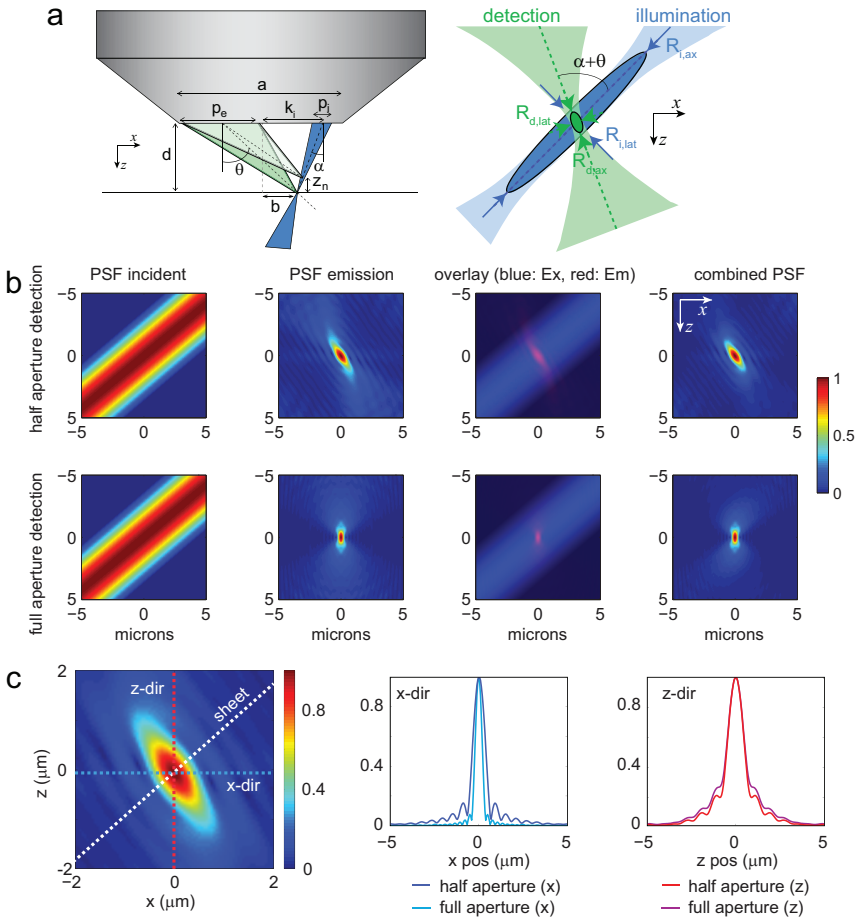

Supplemental Figure 3. Fourier Optics model of the SCAPE PSF. a) defining the imaging geometry of SCAPE. b) An excitation sheet, and a detection point spread function were modeled based on a 20x, 0.95 NA, 2mm WD objective lens, and then combined. Using either the half aperture ($p_e = a/2$) or the full aperture ($p_e = a$) of the objective. We see that at 20x, the NA of the detection side is the dominating factor in the resolution of the system. c) Zoomed in version of Figure 1e, with corresponding plots of the x and z cross-sections indicated for both half and full-aperture detection.

This first Fourier model shows the 'ideal' resolution of the central point of a SCAPE scan, however an important feature of SCAPE's scan pattern is that its resolution will change as a function of the position within the field of view. This is caused by a combination of lens-based aberrations (such as coma), and the crossing angle between the excitation sheet and the effective 'detection cone'. Given the need to simulate scanning beams with high resolutions over large fields of view, to assess these effects we used a simplified PSF model based on rotating Gaussian beams, which primarily captures the effects of crossing angle rather than lens aberrations (although individual points were compared to the Fourier model for validation). Briefly: an excitation beam, with initial diameter p_i and a focal point at z = d (assuming a Plan imaging plane, see Supplemental Figure 4a) was modeled and rotated by angle α. A second 2D Gaussian beam was then also simulated representing the detection (emission) side, with a numerical aperture defined by the aperture p_e, and with its focus intersecting with the excitation beam at z = d once rotated by angle θ. The product of these two beams was then calculated to form the crossed PSF[5]. This process was repeated for detection paths intersecting the illumination beam at locations z_n above and below the focal plane z = d, and for different sets of α and θ values across the scan range. PSFs were generated for three different geometries (a 20 x objective with full, or half detection aperture, and for a 30 mm focal length 1" lens as the objective), at three different scan positions at the extremes of the field of view. This model was also used to assess the FWHM of the PSF in the x and z directions as a function of a large field of view for each of these cases.

The plots in Supplemental Figure 4b show expected crossing angles between the excitation sheet and 'detection cone' for different x-scan positions and depths z_n for a 0.95 NA, 2mm WD objective. Within a usable field of view (FOV) the 'half aperture' configuration maintains a crossing angle close to 90 degrees, which is equivalent to conventional light sheet microscopy. The PSFs shown in Supplemental Figure 4c,d and e demonstrate the predictable effect of scan position on the PSF resulting from changes in the crossing angle between the excitation sheet and the detection cone (note, this model does not account for aberrations or the additional remapping of the PSF in the image rotation arm). Estimated patterns of x and y resolution across the field of view are shown in the maps in f,g and h. In practice, we use a smaller field of view than the range modeled here, for example; owing to clipping of the incident light within the Olympus XLUMPlanFl 20 x/0.95W, we detect little signal for x-positions where b > 0 mm. However, the field of view could feasibly be extended through specialized lens design. The simulation of the 30 mm lens as an objective similarly demonstrates that certain regions of the field of view could yield surprisingly good resolutions over a very large (~ cm) fields of view. SCAPE has been used in this 'macroscopic' imaging configuration to image cleared samples such as whole adult *Drosophila*.

Comparing 'full aperture' to 'half aperture' detection, as predicted by our Fourier model, for high NA objectives, the dominating factor in the system resolution is the NA of the detection side, more than the angle between the excitation sheet and the detection path. Our choice of a polygonal scanning element in our first generation design intentionally limited the numerical aperture of the detection path to maximize the angle between the incident and detected light (Supplemental Figure 4b). However, there is a clear trade-off between maximizing the angle between the two intersecting beam paths ($\alpha+\theta$), versus

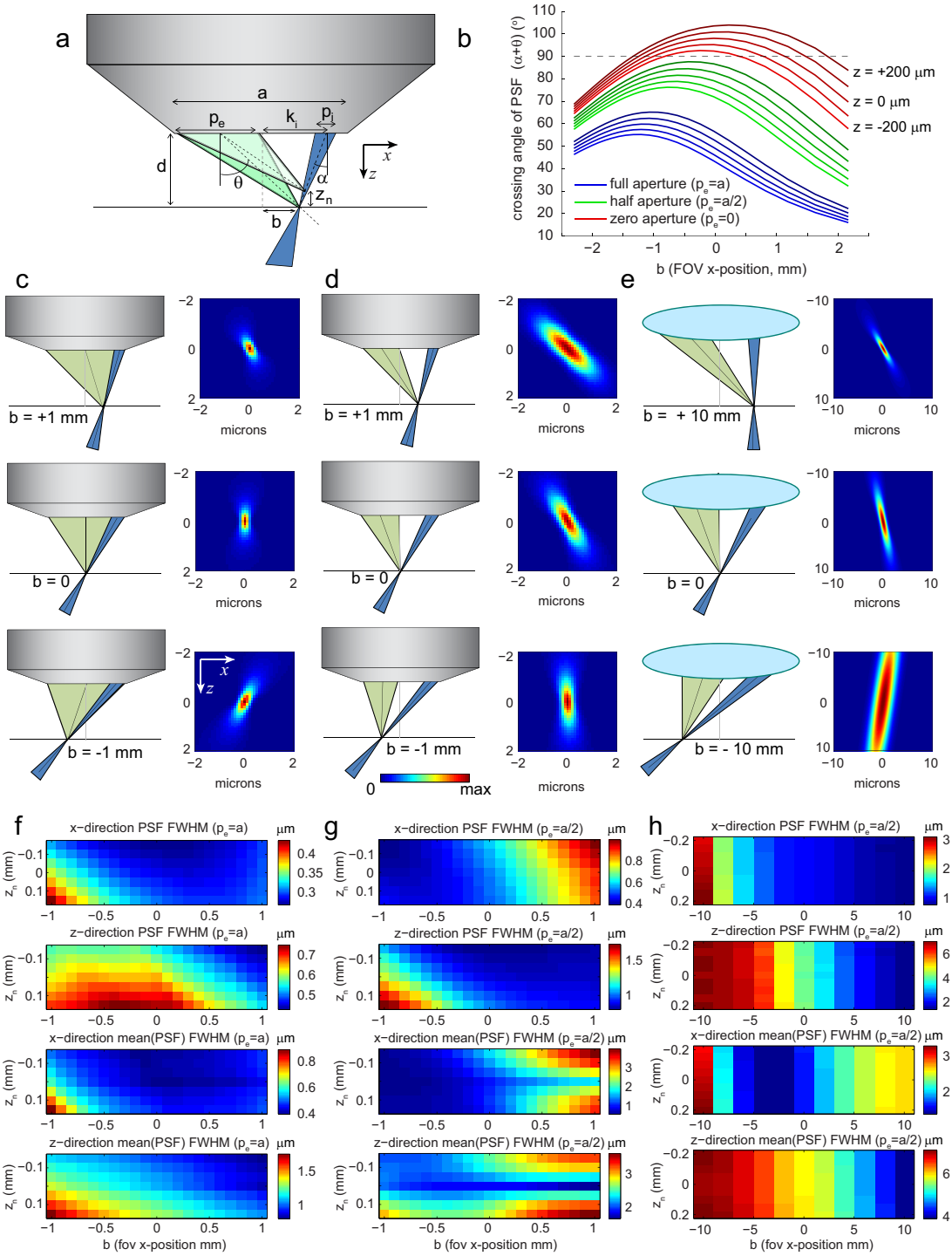

Supplemental Figure 4. Gaussian beam-based simulation of factors affecting SCAPE resolution as a function of position. (a) shows the imaging geometry, (b) shows plots of the effective angle between the excitation sheet and detection 'cone' for different x-direction scan positions assuming the geometry of the Olympus XLUMPlanFl 20x/0.95W objective lens. Columns c,d and e show the imaging geometry and predicted x-z PSFs for three different scan positions, and for three different cases: full aperture detection for the 20x objective (c), half aperture detection for the 20x objective (d) and half aperture detection using a 30 mm focal length, 1" diameter lens. f, g and h show 'resolution maps' as a function of x-z field of view position. The top two maps shown the FWHM of the PSF transecting the focal point across x and z (as defined in Supplemental Figure 3c). The two maps below show the FWHM of the mean PSF in the orthogonal direction.

maximizing the NA of the detected light to improve throughput, lateral and axial resolution. Our simulations show that maximizing the aperture of the detected light has the most significant effect on the system's resolution and depth of field, and would also significantly improve system throughput. We conclude from this modeling that increasing the NA of our detection side would be highly beneficial. One possible alternative system configuration for SCAPE, guided by this model, is shown in Supplemental Figure 5. In this case, the full angle of emitted light would be separated using a dichroic beam-splitter and descanned using a second galvanometric mirror. This configuration would also improve descanning inaccuracies caused by the slight translation that accompanies rotation of a polygon mirror (Supplemental Figure 2). Mirror synchronization is unlikely to be a problem since the mirrors scan at the volume acquisition rate (under 100 Hz). A single planar mirror could also be feasibly used instead of the polygon, with the dichroic placed in the descanned stationary beam path. A third scanner could also be incorporated here to generate the light sheet from a light line, which could be preferable for two-photon implementations of SCAPE.

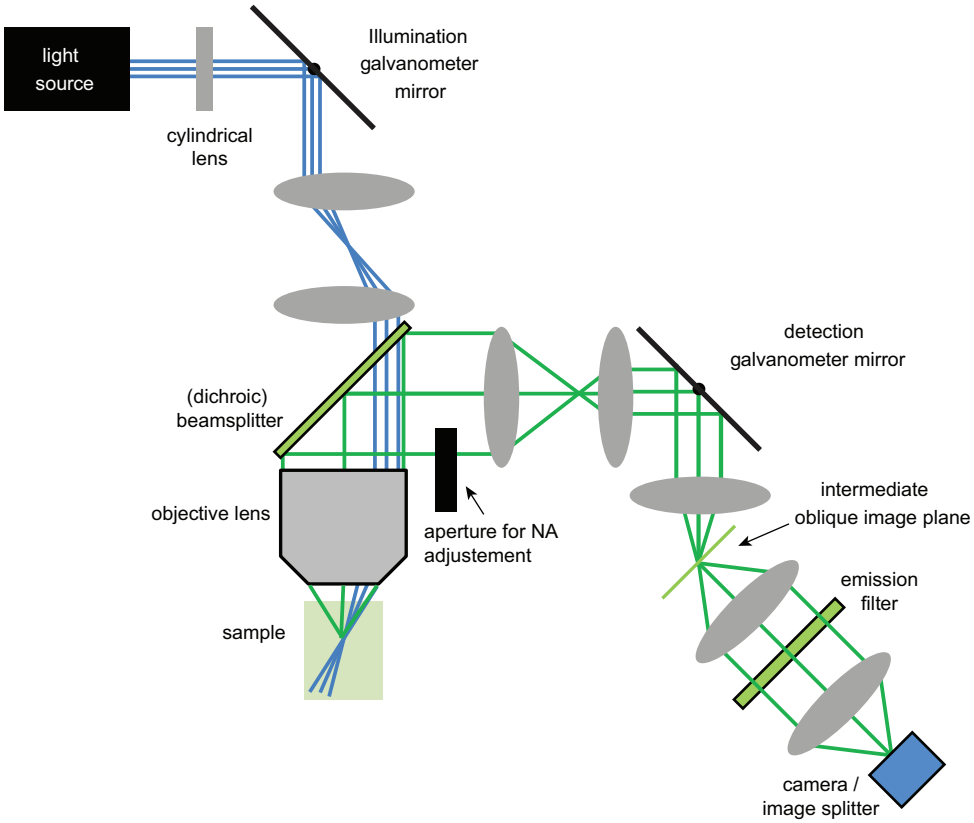

Supplemental Figure 5. Proposed alternative optical design for SCAPE that would allow adjustable detection NA, thereby improving resolution, throughput and depth of field. Illumination and detection scanning mirrors would scan at the volume rate and would be synchronized to provide simultaneous scanning and descanning.

Supplemental Section 2:

Measurements of field of view, resolution, effects of scatter

While the simulations in supplemental section 1 above sought to define the fundamental limit of resolution of SCAPE, a range of phantom measurements were also performed to demonstrate the imaging performance of our current prototype SCAPE system. In most of the in-vivo imaging examples shown in the pain article, the number of depths acquired (corresponding to the number of camera rows and thus the maximum depth measured) was chosen to maximize imaging speed, since the number of rows binned in the camera directly influences the camera read-out rate (see supplemental section 3). The phantom measurements below demonstrate the field of view of our current prototype system in non-scattering versus scattering samples, while also allowing assessment of how close our current resolution performance is to our predicted 'best-case' model.

Phantoms were created using standard green-fluorescent beads with diameters of either 4 microns (F-8859, Life Technologies) or 200 nm (F8811, Life Technologies). Beads were suspended in 1% low-temperature agarose (05073, Fluka), avoiding aggregation. Intralipid-20% (I141, Sigma) was used to add scattering to two of the 200 nm bead phantoms to yield reduced scattering coefficients of μ_s' ~1 mm^{-1} and 2 mm^{-1} at 488 nm (1:36 and 1:18 solutions respectively based on [6,7]). These values were chosen to span the range of reported scattering coefficients in rat and mouse brain [6,8].

Once prepared, agar solutions were cast into small discs by filling a 5 mm inner diameter reservoir glued to a microscope slide and immediately covering with a glass coverslip. The presence of the glass coverslip, as well as the aqueous agar phantom (with added lipid) provides a reasonable approximation in terms of geometry and refractive indices to the cranial window in our awake mouse experiments.

The SCAPE system was configured with an LCPlanFL 20x/0.40NA objective at the image rotation plane (rather than a UPlanFL N 10x/0.30 NA used in some measurements) to maximize magnification of the image onto the camera (reducing field of view, but providing maximal sampling of the system's PSF). The DV-2 image splitter was removed, and all light emerging from the phantoms was captured through a 500 nm long-pass filter. Phantoms were imaged with more 'scan-dimension' (x') steps than in-vivo data, again to capture detail of the system's PSF. Images were acquired to explore both the 3D field of view of the system, as well as the dependence of the system's PSF on depth and scattering.

Field of view:

Supplemental Figure 6 below shows SCAPE measurements acquired to demonstrate the field of view of our current system. A) shows data acquired on 4 micron fluorescent beads in non-scattering agarose. Images are maximum intensity projections over each dimension. Data is shown in SCAPE x', y', z' space, which is not fully Cartesian, as defined in the inset picture. All dimensions were converted to microns via calibration measurements detailed in the supplemental methods section. A scan (x') range corresponding to 600 microns was used and is uniformly filled. The lateral (y') dimension field of view corresponds to the width of the camera sensor, but detected signal is limited by the lateral width of the illuminating light sheet and aperturing of the returning light by detection optics. The usable field of view is

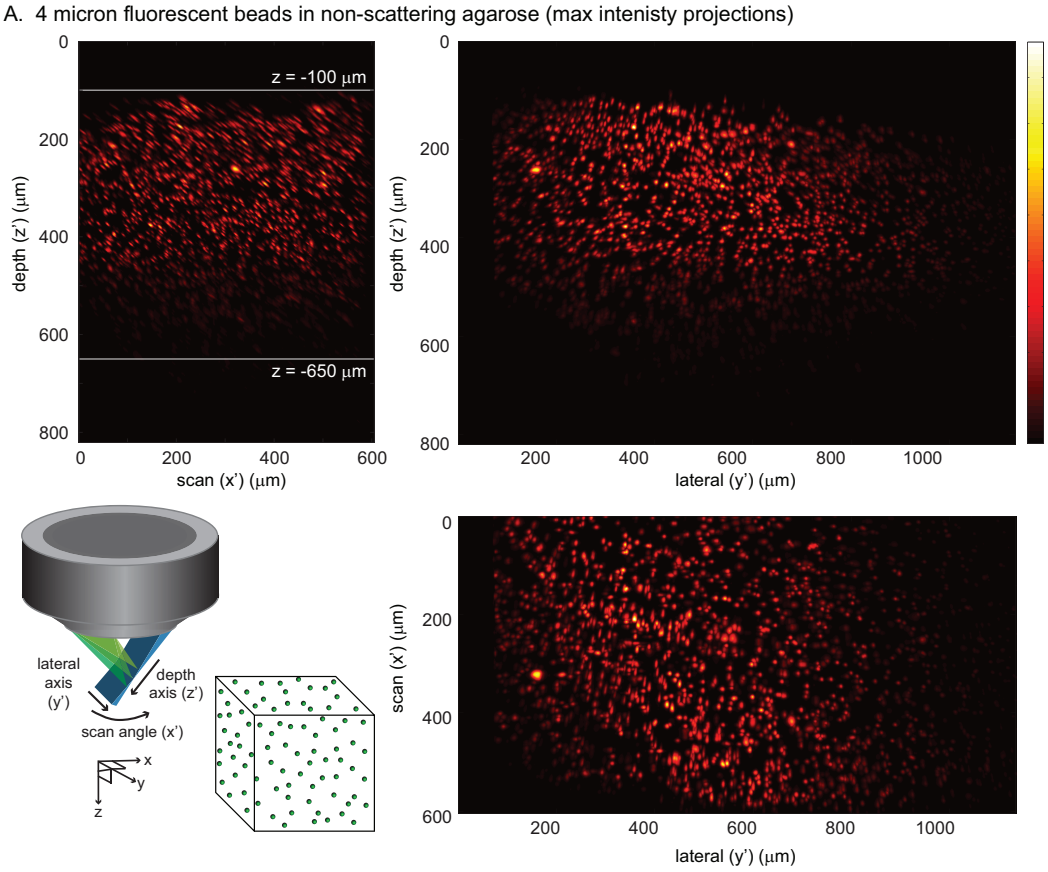

Supplemental Figure 6. SCAPE data acquired on fluorescent bead phantoms. A. Shows maximum intensity projections of data acquired on 4 micron beads. The overall field of view acquired was 600 x 1500 x 820 microns (x'-y'-z', corresponding to 1500 x 1200 x 1500 voxels) with a usable range of around 600 x 1000 x 550 microns. Inset left defines imaging geometry v/s Cartesian space. B. Shows 200 nm beads suspended in agarose with different concentrations of Intralipid™ to provide scattering properties similar to living brain tissue. Images shown are maximum intensity projections over the scan (x') dimension. Background scattering has a marked effect on the achievable penetration depth for imaging.

thus around 1 mm in the configuration shown. The depth (z') axis was acquired with a large number of camera rows to demonstrate achievable penetration depth. Imaging depth is limited by both attenuation and scattering of excitation and emitted light, as well as aperturing of light in the detection beam path. A usable range of around 550 microns is demonstrated in this configuration.

Another important effect is visible in the z'-x' projection. As explored further in Supplemental Figure 8 below, and consistent with our modeling results, the thickness of the light sheet causes some diagonal stretching of the imaging point spread function (PSF) above and below the focal plane of the light sheet (x'–z' panel in A). In low-scattering samples, maximum penetration depth can be achieved by positioning the focal plane below the surface of the sample, such that the best resolution is at the center of the z' field of view. Here, the best focal range is around 200-400 microns below the surface of the sample such that diagonal PSF stretching is seen at the surface, and in deeper sections. We note that these images show minimal effects from the de-scanning imperfections and field curvature predicted by our modeling of real lenses in Supplemental Figure 2.

Panel B shows data acquired in 200 nm bead phantoms where different levels of scattering were added to the agarose background. Scattering causes additional signal decay with depth due to broadening of the light-sheet as well as losses in detected light traveling to and from deeper layers. The usable penetration depth for a reduced scattering coefficient of ~ 1 mm^{-1} is found to be around 250 microns, while at $\mu_s' \sim 2\ mm^{-1}$, this reduces to 150-200 microns. While the data in the non-scattering phantom was acquired by positioning the focal plane of the light sheet around 250 microns below the surface, data in the scattering phantoms was acquired with the focal plane closer to the surface of the sample, which sacrifices some depth penetration but maximizes signal and resolution within the usable field of view. It should be noted that the images shown here were acquired using a 488 nm laser source. Scattering levels in tissue at 488 nm are very high, a feature that has limited the use of standard confocal microscopy in living tissues. Since scattering in tissue is exponentially lower at longer wavelengths (approximately following $\mu_s' = A\lambda^{-b}$) implementation of SCAPE at longer excitation wavelengths (e.g. > 600 nm, or even near infra-red) would be expected to provide greatly enhanced penetration into scattering tissues. Optimization of alignment, NA and throughput would also improve signal to noise at deeper depths, extending the usable range.

Penetration depth quantification in in-vivo brain tissue

As a further demonstration of the effects of in-vivo brain optical properties on SCAPE penetration depth and resolution, we performed comparative imaging using SCAPE and two-photon microscopy in the in-vivo mouse brain after intravenous injection of dextran conjugated fluorescein (see methods). Intravenous labeling provides structures throughout the depths of the cortex, with deeper capillaries on the order of 5-10 microns in diameter being filled with dye of uniform concentration (providing similar targets to the fluorescent beads imaged above). For animal preparation see methods, for imaging parameters and alignment see supplemental methods.

Figure 2e in the main text shows side by side comparisons of x-y planes acquired with SCAPE and two-photon microscopy at 4 different depths. Supplemental movie 2 shows the

same data set as a full sequence of z-planes between the modalities down to 200 microns in depth. Supplemental Figure 7 below further compares the two data sets as a function of depth, displaying maximum intensity projections over x-z and y-z in approximately the same planes in both the two-photon and SCAPE data. In this case only, a high-pass filter (Matlab™ 'unsharp') was applied remove diffuse background from the SCAPE data (visible in Figure 2e and Supplemental Movie 2), in order to improve maximum intensity projections. Each depth plane was also normalized to its own mean for both techniques; for the two-photon data to account for the 4 discrete increases in laser power required to cover the range of depths, and for SCAPE to account for the gradual attenuation of signal with depth.

This comparison demonstrates that SCAPE can provide near-isotropic resolution in-vivo, revealing capillary loops in superficial cortical layers with similar performance to two-photon microscopy. At deeper depths (>200 microns) the larger diving arterioles and ascending venules are still resolved, in fact SCAPE provides much stronger contrast for these axially oriented structures than two-photon microscopy, in part because angled SCAPE illumination avoids the attenuation of signals from vessels diving directly beneath surface vessels (as can be seen in the two-photon images in Figure 2e). Larger diving vessels can be resolved to depths of around 300 microns in-vivo using 488 nm excitation. Near-identical contrast and signal to noise was seen with 6x more power and a 340 Hz frame rate, yielding 10 VPS at with 34 angular steps. Again, longer wavelengths, and potentially two-photon implementations of SCAPE are expected to improve this penetration depth performance significantly.

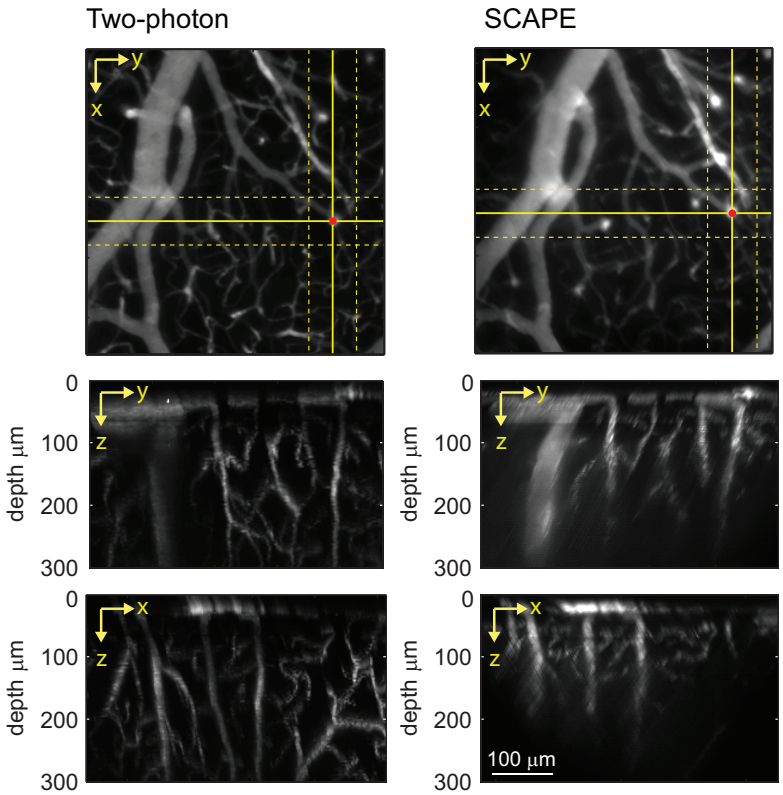

Supplemental Figure 7. Two-photon v/s SCAPE comparison of depth-dependent imaging of in-vivo mouse brain vasculature. Top: mean intensity projection of the top 150 microns of the stack for each modality. Dotted yellow lines show the range over which maximum intensity projections were calculated along each dimension. Below: maximum intensity projections for x-z and y-z planes for each data set as indicated. Capillary loops in the x-z and y-z planes can be seen clearly in more superficial layers of the SCAPE data. Deeper structures such as diving arterioles and ascending venules are resolved by SCAPE down to depths of almost 300 microns using 488 nm illumination.

Resolution and the effects of scatter

Supplemental Figure 8 below shows a more detailed resolution analysis of SCAPE data acquired on 200 nm beads in a non-scattering (top) and a $\mu_s' \sim 1\ mm^{-1}$ scattering phantom (bottom). Since the system's PSF is spatially variant (as predicted by our simulations), rather than averaging we show raw, single-bead PSFs for a range of beads at different depths in each phantom as indicated. Cross-sections through each PSF are shown to the right, with full width half maxima (FWHM) noted. As before, dimensions are converted to microns based on our calibration procedure, but data is shown in x'-y'-z' space at its native sample resolution.

Several interesting features can be observed. Firstly, the x'-y' and y'-z' PSFs look generally circular, with some distortions owing to aberrations such as coma in our non-optimized optical path. The x'-z' projections show the slightly elongated, diagonal shape predicted in our simulations, which is caused by the light sheet thickness and the relatively low NA detection of our current prototype system. As expected, this PSF shape changes as a function of depth, corresponding to the narrowing of the light sheet towards its focal plane. Our simulations predict that this distortion would improve with higher NA detection.

It should be noted that the relative resolution in all dimensions can be varied based on alignment. For these measurements, we used less of an aperture to block coma aberrations in order to maximize the field of view, causing the y' dimension to be broadened at the expense of improved x' and z' resolution. Mis-alignment of the image rotation optics can also cause depth-dependent aberrations and loss of single, and can never be perfect in our current system owing to expected field curvature as predicted by our modeling in Supplemental Figure 2.

Data in the scattering sample shows reduced signal at deeper depths, as expected. However, it is interesting to note that scattering does not appear to have a marked effect on the system's resolution. We conclude this based on the PSF of the deepest bead in both phantoms, which exhibits distortions likely due to light-sheet aberrations, field curvature and imperfections in detection optics. While this deepest PSF in the scattering phantom is sampled from a shallower depth than in the non-scattering phantom, its position is consistent with the shallower position of the light sheet focal plane in the scattering sample, as described above. The depth at which this aberration occurs is essentially consistent between the two samples, such that it cannot be the result of light scattering. We conclude that within this length scale, the dominant effect of scattering is to reduce detectable signal, rather than to introduce blurring, again suggesting the longer-wavelength and two-photon implementations of SCAPE will provide significant benefits for imaging scattering samples.

In both samples, the resolution of our current system is found to be between 2-3 microns in most cases (with aberration in y' leading to 4-7 micron resolution), over a large field of view. We anticipate that this resolution can be improved with custom optics, optimized alignment and higher NA detection. However, it should also be noted that the sample density of data shown in the rest of the manuscript is lower than the sample density used here, in order to optimize volumetric frame rate and field of view for in-vivo imaging. For example, the data shown in Figure 3 used 240 x 200 x 40 voxels x'-y'-z' to sample a 600 x 650 x 134 micron field of view such that each voxel corresponded to 2.5 x 3.25 x 3.6 microns x'-y'- z' respectively, making our chosen voxel size similar to our current system's optical PSF.

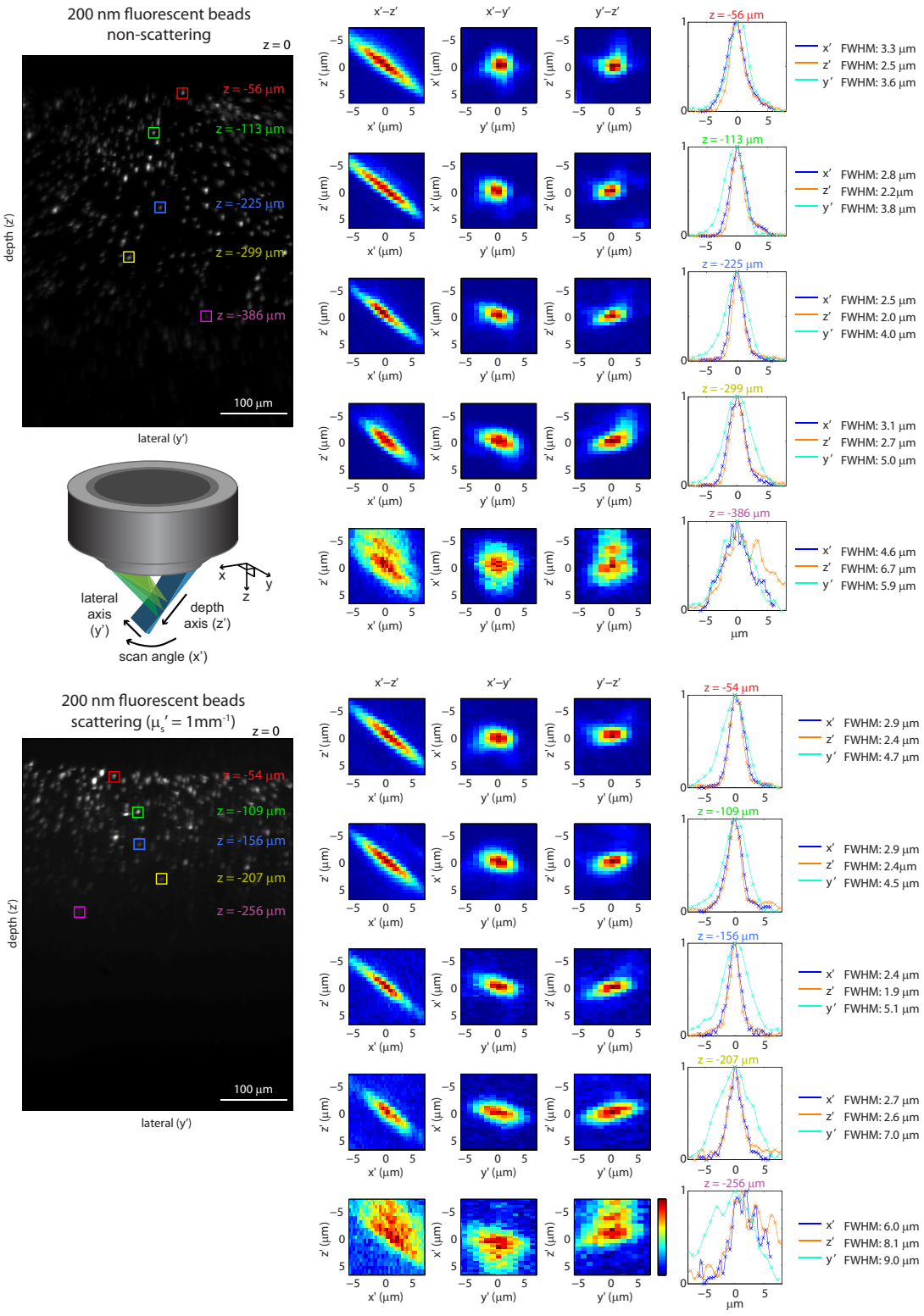

Supplemental Figure 8. Point spread function analysis for our current SCAPE prototype in 200 nm beads for non-scattering and scattering samples. Panel to the left shows a mid-scan y'-z' plane as a maximum intensity projection over a 20 micron thick section. Beads selected for PSF analysis are indicated by colored boxes. Maps show single planes of SCAPE data through the peak voxel of each bead in each dimension. Plots to the right show cross-sections through the center point for each dimension (spline interpolations through measured points indicated by x's. The FWHM of each curve is indicated to the right.

Supplemental Section 3:

Volumetric imaging speed analysis

Since the only moving component of SCAPE is a slowly scaning mirror, the system's imaging speed is limited primarily by camera frame-rate (and ultimately, signal to noise). The volumes per second (VPS) rate for a given acquisition is the camera's frame-rate divided by the number of x' direction angular steps desired in the volume. The different parameters used for the data shown in this paper are shown below:

Figure	Camera y'- z' FOV (pixels)	# Angular steps (x')	Camera fps	VPS	Pixel rate (MHz)
2	1400 x 80 (2-color, 500 wide each)	100	1000	10	40
3	400 x 40 (2x2 binning)	240	2404	10	38.5
4	800 x 80 (1x1 binning)	120	2404	20	153.9
5a	700 x 100 (2-color, 300 wide, 2x2 binning)	100	1000	10	70
5d	660 x 100 (2-color, 240 wide, 2x2 binning)	80	800	10	52.8

Volumetric imaging speed can be increased by choosing fewer angular steps (x') for each volume, which will either reduce the sampling density, or field of view along the x' axis, depending on the corresponding angular range. Binning cameras to acquire less rows can also significantly increase their frame rates, up to 2404 fps for 80 rows = depths for our current Andor Zyla sCMOS camera. Importantly, faster cameras are commercially available that could go beyond the speeds demonstrated here. The NAC Memrecam HX-3, for example, can sample 384 x 288 frames at 75,000 fps, which could yield 375 vps for a field of view with 200 lateral sampling steps, assuming adequate signal to noise.

Ultimately then, the speed limit of SCAPE will be governed by the signal-to-noise achievable at the very low integration times required for very high frame rate acquisition. Performance will therefore be a trade-off between the camera's sensitivity and noise levels, the efficiency of the fluorophore in the sample, available laser power and the ability of the sample to withstand illumination intensities high enough to yield images of sufficient quality. This limit is therefore sample dependent, and will be determined by the chosen application of the system. This sample-dependent fundamental volumetric scan rate limit applies to all optical imaging systems, although SCAPE shares the feature of all light-sheet imaging approaches in that it should minimize photodamage compared to confocal and wide-field fluorescence imaging.

Our prototype SCAPE system demonstrated here used a relatively inexpensive sCMOS camera with small 7 x 7 μm pixels, and had reduced throughput owing to the detection aperturing. Nevertheless, we saw only minimal evidence of photobleaching or phototoxicity when imaging living samples. We therefore anticipate that improving throughput, using higher laser powers and cooled cameras with larger pixel sizes in combination with increasingly bright and stable in-vivo fluorophores will readily enable practical SCAPE volumetric scan rates exceeding 50 VPS in typical biological samples.

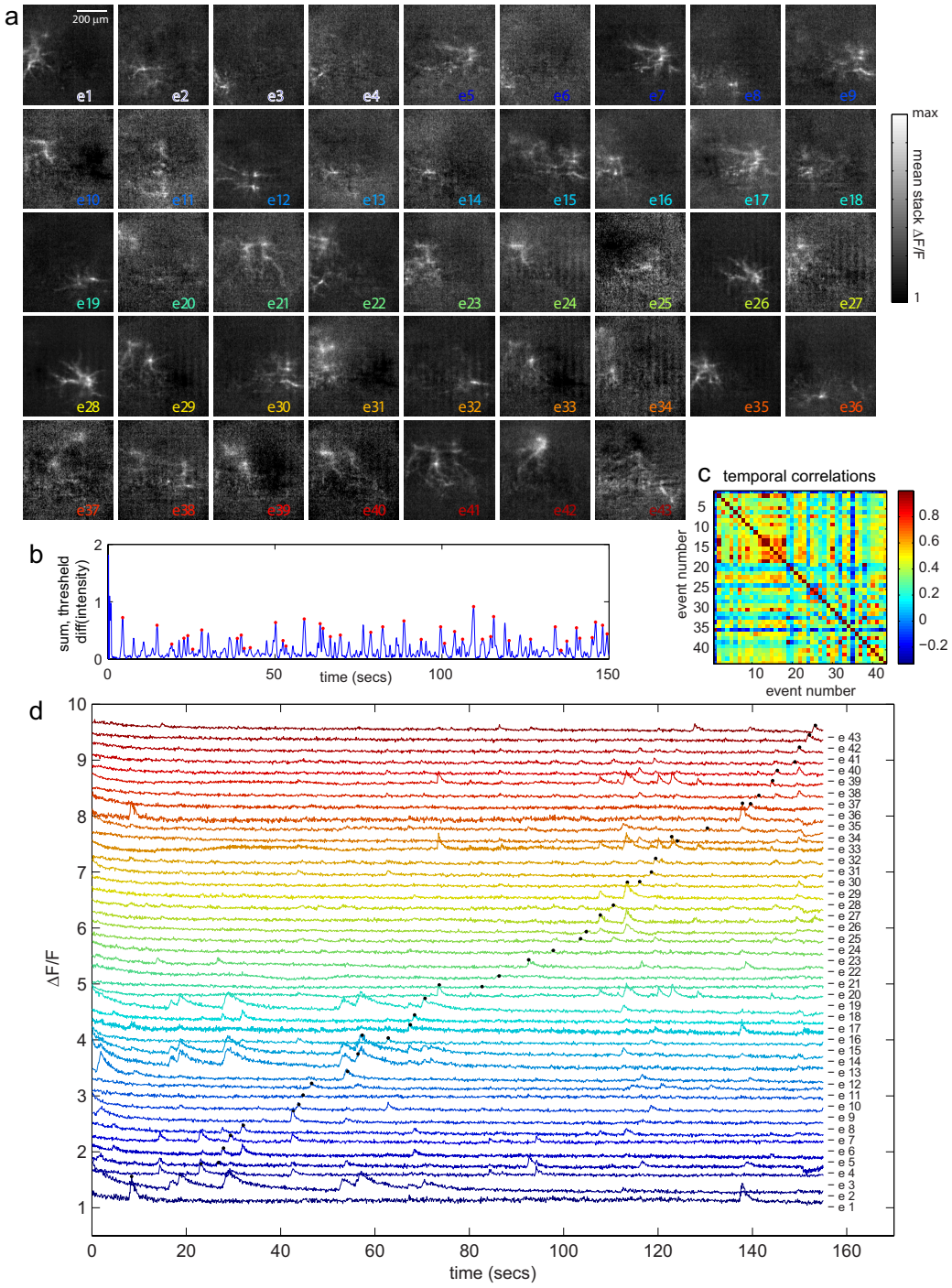

Supplemental Figure 9. SCAPE data showing spontaneous neuronal firing in the awake behaving mouse brain. Additional analysis of the firing events within the data set shown in Figure 3 shows many, distinct events. Neuronal events were initially identified by searching the data for events in which subsets of pixels exceeded a threshold value (panel b). The images in (a) show mean intensity depth projections of the difference image corresponding to each of these different events, revealing expected lateral dendritic structures in unique patterns (in some cases the same pattern can be seen, corresponding to the same neuron firing again). Signal was extracted from the peak x'-y'-z' voxel within each of these neuronal even maps, and these time-courses are shown as raw signal traces in (d), with a black dot representing the event at which the time-course was selected. (c) shows a correlation map of these time-courses, which correctly identifies when events correspond to the same neuron firing repeatedly, versus novel events.

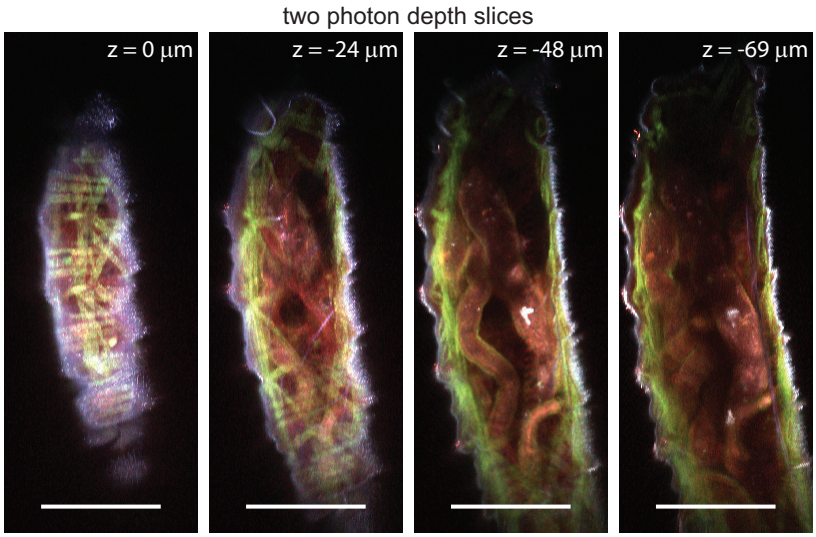

Supplemental Figure 10. Reference two-photon microscopy images of a 1st instar MHC-GFP *Drosophila* larva (compare to SCAPE images in Figure 4 and Supplemental Movies M4 and M5). Expression of GFP in the body muscles and gut smooth muscle can be seen, along with autofluorescence of food and second harmonic generation (blue) in the outer cuticle. Scale bars 200 μm.

Supplemental Information references

1 Tsai, P.S. *et al.* Principles, design and construction of a two photon scanning microscope for in vitro and in vivo studies. *Methods for In Vivo Optical Imaging (R. Frostig, editor)* **CRC Press**, 113-171, (2002).

2 Dunsby, C. Optically sectioned imaging by oblique plane microscopy. *Opt Express* **16**, 20306-20316, (2008).

3 Radosevich, A.J., Bouchard, M.B., Burgess, S.A., Chen, B.R. & Hillman, E.M. Hyperspectral in vivo two-photon microscopy of intrinsic contrast. *Opt Lett* **33**, 2164-2166, (2008).

4 Pankajakshan, P. *et al.* in *Signals, Systems and Computers (ASILOMAR), 2010 Conference Record of the Forty Fourth Asilomar Conference on.* 1364-1368.

5 Engelbrecht, C.J. & Stelzer, E.H. Resolution enhancement in a light-sheet-based microscope (SPIM). *Optics Letters* **31**, 1477-1479, (2006).

6 Hillman, E.M. Optical brain imaging in vivo: techniques and applications from animal to man. *J Biomed Opt* **12**, 051402, (2007).

7 Van Staveren, H.J., Moes, C.J., van Marie, J., Prahl, S.A. & van Gemert, M.J. Light scattering in Intralipid-10% in the wavelength range of 400-1100 nm. *Applied optics* **30**, 4507-4514, (1991).

8 van-der-Zee, P. *Measurement and modelling of the optical properties of human tissue in the near infrared*, University College London, (1992).